Efficient photo-switchable activation of periodate by nitrogen-vacancy-rich carbon nitride for organic contaminant removal: Theoretical predictions and experimental validations

Yi-Jiao Sun [a], Zhuo-Ya Fang [a], Xin-Tong Huang [a], Chang-Wei Bai [a], Ke-An Zhu [a], Xin-Jia Chen [a], Bin-Bin Zhang [a], Yi-Shuo Zhang [a], Qi Yang [b,c], Jie-Xuan Zheng [d], Fei Chen [a,*]

[a] *Key Laboratory of the Three Gorges Reservoir Region's Eco-Environment, Ministry of Education, College of Environment and Ecology, Chongqing University, Chongqing 400045, China*
[b] *College of Environmental Science and Engineering, Hunan University, Changsha 410082, China*
[c] *Key Laboratory of Environmental Biology and Pollution Control (Hunan University), Ministry of Education, Changsha 410082, China*
[d] *College of Chemistry, Soochow University, Soochow 215006, China*

ARTICLE INFO

ABSTRACT

This study presents a simple N_2 calcination method at various temperatures to achieve nitrogen-vacancy-rich g-C_3N_4 for periodate (IO_4^-) activation under visible light. The developed system demonstrated remarkable effectiveness in eliminating various organic pollutants. Especially, bisphenol A, the model pollutant, could be completely removed within 30 min, exhibiting an activity 9.37 times higher than that of the background activator. Theoretical calculations suggest that small active molecules, including contaminants and oxidants, showed a higher affinity for adsorption onto the g-C_3N_4 surface in the presence of nitrogen vacancies. This promoted sufficient electron supply and rapid electron transfer, enhancing IO_4^- activation during decontamination. Furthermore, we comprehensively examined the evolution of reactive species, such as $IO_3^{\bullet}$, $^{\bullet}O_2^-$, $^1O_2$, $^{\bullet}OH$, and h^+, and explored the application potential of the catalytic system. This work provides new insights into the design of photo-self-cleaning IO_4^- activators and highlights this method's potential for application in other oxidation systems.

1. Introduction

Water pollution has become a severe issue in recent years, with persistent organic compounds in wastewater posing a significant threat to ecosystems and human health [1–4]. This calls for the development of efficient and eco-friendly technologies for wastewater purification [2,5]. The advanced oxidation process activated by periodate (PI, IO_4^-) has emerged as a promising method for rapid pollutant decontamination, as it can generate various robust oxidative species in situ, including iodyl radicals ($IO_3^{\bullet}$), hydroxyl radicals ($^{\bullet}OH$), superoxide anion radicals ($^{\bullet}O_2^-$), singlet oxygen ($^1O_2$), etc [6–9]. However, despite its strong oxidizing power ($+1.6$ V), IO_4^- alone struggles to remove organic contaminants [10–12] effectively. Therefore, developing highly active, scalable, and eco-friendly heterogeneous activators is crucial to enhance the practicality of this technology compared to homogeneous systems.

Extensive research has been conducted on various heterogeneous activators, with transition metal-based catalysts being widely recognized as the most promising due to their excellent activation performance and cost-effective nature [10]. For example, iron (Fe)- [11–14] and manganese (Mn)- [15–18] based catalysts have demonstrated efficient IO_4^- activation, resulting in the generation of reactive species that enable rapid pollutant removal from wastewater. However, these activators are prone to metal precipitation in catalytic systems, particularly under acidic conditions, compromising their stability and long-term applicability in continuous reactions. On the other hand, carbon-based activators can address these issues, but conventional carbon materials require a regeneration step after reactions, leading to increased costs and process complexity. Interestingly, certain carbon-based materials possess unique properties, such as visible light responsiveness, eliminating the need for regeneration [19,20]. These catalysts can undergo self-cleaning through photocatalytic production of active species under direct visible light following the catalytic reaction. Thus, selecting an

appropriate carbon-based visible light-responsive material as an IO_4^- activator is an optimal choice.

Carbon nitride (g-C$_3$N$_4$), a metal-free material, has gained significant attention in the field of photocatalysis due to its narrow band gap (~2.7 eV), allowing for efficient utilization of visible light, as well as its desirable properties such as simple preparation, stable physical and chemical characteristics, and scalability [21–24]. Its potential in activating various emerging oxidants has been extensively explored, highlighting its high value in applications [25–27]. Previous studies have demonstrated that bulk g-C$_3$N$_4$ can activate IO_4^- with the aid of visible light, resulting in the rapid removal of tetracycline [28]. These findings suggest that g-C$_3$N$_4$ is a promising carbon-based substrate for activating IO_4^-. However, bulk g-C$_3$N$_4$ monomers tend to exhibit slow charge separation kinetics and secondary carrier recombination, which significantly limits their ability to activate oxidants. Given that g-C$_3$N$_4$ is primarily composed of C-N bonds, it is prone to forming defects (C or N) [29–31] in its structure, providing an opportunity to modify its intrinsic photoelectric properties significantly. Among these defects, nitrogen vacancies (Nv) [32–34] have been identified as particularly influential in creating new defect energy levels, enhancing visible light absorption, accelerating carrier separation, and promoting the accumulation of photogenerated holes. Consequently, we aimed to modulate the Nv concentration in g-C$_3$N$_4$ by adjusting the temperature in an N$_2$ atmosphere, thereby creating an ideal activator for IO_4^- and accelerating the decontamination process under visible light irradiation. However, there is a gap in our understanding regarding the relationship between Nv concentration, IO_4^- activation performance, and the rate of organic pollutant removal, which needs to be investigated. Furthermore, the regulation of active species in this system and a comprehensive validation of their changes require thorough investigation.

With these objectives in mind, we employed a secondary N$_2$ calcination method to modulate the formation of nitrogen vacancies (Nv) and control their concentration on g-C$_3$N$_4$ substrates at various temperatures. Subsequently, we utilized a visible light switch to activate IO_4^- and conducted efficient decontamination of various types of contaminants. Furthermore, we conducted extensive investigations on the optimized parameters, evaluated the system's performance in different environmental applications, analyzed product degradation, and examined the evolution patterns of toxicity. To gain a deeper understanding, we utilized a combination of capture experiments, probe techniques, characterization of photoelectric properties, and theoretical calculations to analyze the types of active species and elucidate the intrinsic mechanism. The findings from this study serve as an experimental basis and provide application support for the future design of a scalable and precisely designed heterogeneous IO_4^--activated system.

2. Experimental section

2.1. Chemicals and reagents

Dicyandiamide (C$_2$H$_4$N$_4$), bisphenol A (BPA), rhodamine B (RhB), tetracycline hydrochloride (TC), ciprofloxacin (CIP), sulfamethoxazole (SMX), atrazine (ATZ), 2,2,6,6-tetramethyl-4-piperidinyl (TEMP), 4-Hydroxy-TEMPO (TEMPOL), tetramethylpiperidine-nitrogen oxide (TEMPO), ascorbic acid (C$_6$H$_8$O$_6$), ethylenediaminetetraacetic acid disodium salt (EDTA-2Na), *tert*-butyl alcohol (TBA), hydrogen peroxide (H$_2$O$_2$, 30 wt%), *L*-histidine (C$_6$H$_9$N$_3$O$_2$), p-benzoquinone (BQ), ethanol, periodate (PI, IO_4^-), hydrogen peroxide (H$_2$O$_2$), peroxymonosulfate (PMS), peroxydisulfate (PDS), humic acid (HA), sodium carbonate anhydrous (Na$_2$CO$_3$), sodium chloride (NaCl), sodium sulfate anhydrous (Na$_2$SO$_4$), sodium nitrite (NaNO$_2$), sodium nitrate (NaNO$_3$), magnesium chloride (MgCl$_2$), calcium chloride (CaCl$_2$), acetonitrile, acetic acid, and formic acid were all purchased from Macklin Chemical Reagent Co., China, Sinopharm Chemical Reagent Co., China, Sigma-Aldrich Chemical Reagent Co., China or Shanghai Chemical Reagent Co., China. All solutions were prepared with Milli-Q water with an 18.25 MΩ/cm

resistivity. The NaOH or HClO$_4$ adjusted the pH value of the solution.

2.2. Characterizations

X-ray powder diffraction patterns of the as-prepared catalysts were recorded with a Bruker D8 advanced X-ray diffractometer (XRD) with Cu Kα X-ray irradiation at 40 kV and 40 mA (Bruker D8 advance Co., Germany). Scanning electron microscopy (SEM) images were collected using a Zeiss Sigma 300 microscope (Zeiss Co., Germany). Transmission electron microscopy (TEM) with a JEOL JEM2100 (JEOL Co., Japan) was used to analyze the surface morphology of different catalysts. Different catalysts' UV–vis diffuse reflectance spectra (UV–vis DRS) were measured by a UV3600-plus spectrometer (Shimadzu Co., Japan) at 200–800 nm. The valence states of the constituent elements were measured by X-ray photoelectron spectroscopy (XPS) using an ESCALAB 250Xi spectrometer (Thermo Fisher Inc., USA). The specified surface areas were obtained using a Brunauer-Emmett-Teller (BET) method with a Builder 4200 instrument (Tristar II 3020 M, Micromeritics Co., USA). The surface properties were analyzed using Fourier transform infrared spectroscopy (FTIR, Nicolet Is10, Thermo Fisher Inc., USA). The ultraviolet-visible diffuse reflectance spectroscopy (UV–vis DRS, UV3600-plus, Shi., Japan) was conducted on a UV3600-plus spectrometer in the range of 250–800 nm. An FLS-1000 fluorometer obtained the photoluminescence (PL, Fluorolog-3, Ho., Japan) and time-resolved PL spectra. The electron spin resonance (ESR) signal spin-trapped by the reagent 5, 5-dimethyl-L-pyrroline N-oxide (DMPO), tetramethylpiperidine-nitrogen oxide (TEMPO), and 2,2,6,6-Tetramethyl-4-piperidone (TEMP) with an ESR spectrometer (ER200-SRC, Bruker Co., USA) was used to reconfirm the generated reactive species during the catalytic reaction. A CHI660E electrochemical workstation equipped with a standard three-electrode system (a saturated Ag/AgCl electrode as the reference electrode, a platinum wire as the counter electrode, and the catalysts-coated FTO glass as the working electrode) was adopted to analyze the photoelectric properties of the prepared catalysts. Total organic carbon (TOC) results were obtained on a TOC-VCPH analyzer (Multi N/C 2100, AG., Germany). The acute and chronic toxicity predictions of the BPA molecule and its intermediates were examined using the Ecological Structure-Activity Relationships (ECOSAR) system.

2.3. Synthesis of nitrogen-vacancy-rich g-C$_3$N$_4$ and control samples

Bulk carbon nitride (g-C$_3$N$_4$, CN-bulk) was prepared by thermal polymerization. Typically, 12 g of dicyandiamide were placed in a covered crucible wrapped in tin foil and transferred to a muffle furnace. The reagent was heated to 550 °C at a heating rate of 2.5 °C•min^{-1}, and stabilized for 4 h. After cooling to room temperature, the pale-yellow CN-bulk was ground and collected for subsequent experiments.

A simple secondary calcination method was used to introduce nitrogen vacancies (Nv) into CN-bulk (CN-Nv). Typically, two parts of 1 g CN-bulk powder were evenly dispersed in two open crucibles and placed in a tubular furnace. The samples were calcined at different temperatures for 2 h at a rate of 2.5 °C/min. The resulting samples were labeled as CN-Nv-x (x = 350, 450, 550, and 650, corresponding to the calcination temperatures of 350, 450, 550, and 650 °C, separately). The optimal secondary calcination temperature was determined through degradation experiments, and the materials were subsequently calcined at the optimal temperature for different durations at a rate of 2.5 °C/min. The obtained samples were recorded as CN-Nv-550-y (y = 0.5, 1, 2, 4, 8, corresponding to the calcination time of 0.5, 1, 2, 4, 8 h, respectively).

Unless otherwise specified, CN-550 or CN-Nv-550 refers to the Nv-containing g-C$_3$N$_4$ material obtained by secondary calcination at 550 °C for 2 h.

2.4. Evaluation of activation performance

All degradation experiments were carried out in a 50 mL reactor equipped with a xenon lamp (PLS-FX300HU, Beijing Perfectlight Technology Co., Ltd.). The reactor was maintained at a temperature of 20 ± 2 °C using circulating water and stirred during the experiments. The reactor was initially filled with 5 mg/L of bisphenol A (BPA) and 0.2 g/L of catalyst in each experiment. The mixture was stirred to establish an adsorption-desorption equilibrium. Subsequently, 1 mM sodium periodate (PI, IO_4^-) was rapidly added to the reactor while the visible light was turned on to initiate the reaction. At predetermined time intervals, 1 mL of the reaction sample was withdrawn, and the reaction was immediately quenched by adding 20 µL of ascorbic acid (0.1 mL, 400 mM). The residual concentration of micropollutants and the conversion products were analyzed using high-performance liquid chromatography (HPLC) and liquid chromatography-mass spectrometry (LC-MS) techniques. Indeed, considering optical properties of different photocatalysts using a six-flux model and relevant parameters, such as the total rate of photon absorption (TRPA), the local volume rate of photon absorption (LVRPA), and optical thickness (τ_{app}) was crucial for a comprehensive understanding of photocatalytic processes[35–38]. By quantifying these optical properties (Text S4), we could gain insights into the efficiency of photon absorption and the overall performance of photocatalysts in degradation. This information was valuable for optimizing the design and enhancing the performance of photocatalysts, ultimately leading to more efficient photocatalytic systems for environmental remediation and other applications.
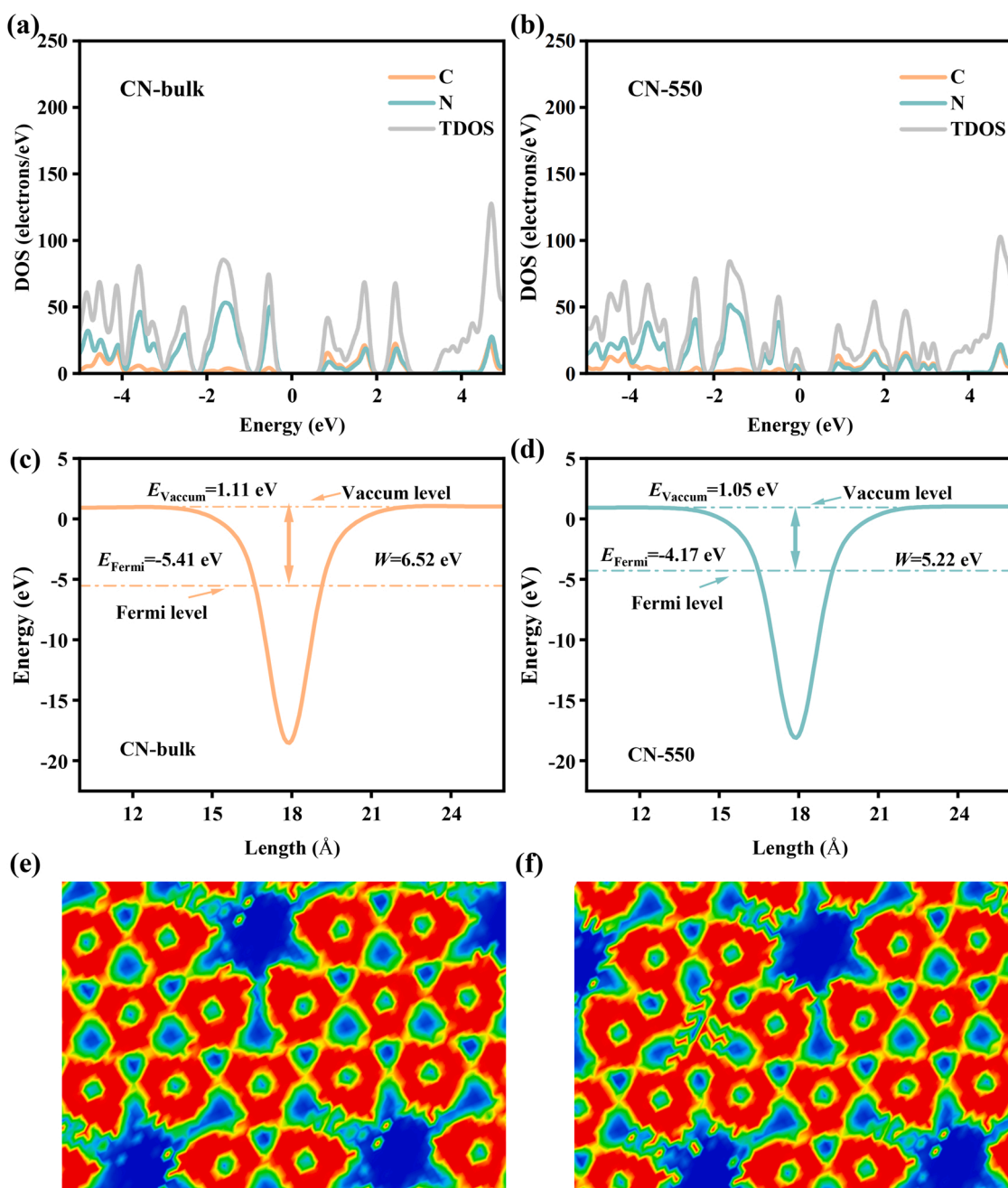

Fig. 1. Multiple predictions of Nv-rich g-C₃N₄. a, b, Density of states: (a) CN-bulk and (b) CN-550. c, d, Work functions: (c) CN-bulk and (d) CN-550. e, f, Two-dimensional charge density: (e) CN-bulk and (f) CN-550, respectively.

2.5. Analytical methods

The concentrations of contaminants were detected on an Agilent 1260 Infinity HPLC with a UV detector and a ZORBAX SB C-18 (5 μm, 4.6 × 250 mm) column at 35 ± 1 °C. The mobile phase was a mixture of acetonitrile and 0.2% acetic acid water (60: 40, v/v). The samples were analyzed at a flow rate of 1.0 mL•min^{-1}, and the injection volume was set as 20 μL. The detection wavelength was 273 nm, and the analysis time was 3.5 min. The formed products of BPA degradation were analyzed by a liquid chromatography-mass spectrometry (LC-MS) system equipped with a 6460 HPLC (Agilent Inc., USA, with a Kromasil C18 column (4.6 ×250 mm)) and an API 3000 mass analyzer. Other

conditions coincided with BPA concentration measurement.

2.6. Density Functional Theory (DFT) calculations

The DFT calculations were conducted using the "Vienna ab initio simulation package" (VASP5.4), applying a generalized gradient correlation functional. A plane-wave basis set with cut-off energy 400 eV within the framework of the projector augmented wave method was employed. The Gaussian smearing width was set to 0.1 eV. The Brillouin zone was sampled with a 3 × 3 × 1 K point. Al1 atoms converged to 0.01 eV•Å^{-1}. An electronic localization function was performed. The adsorption energies (E_{ads}) were defined as $E_{ads} = E_{tot}-(E_s + E_m)$, where
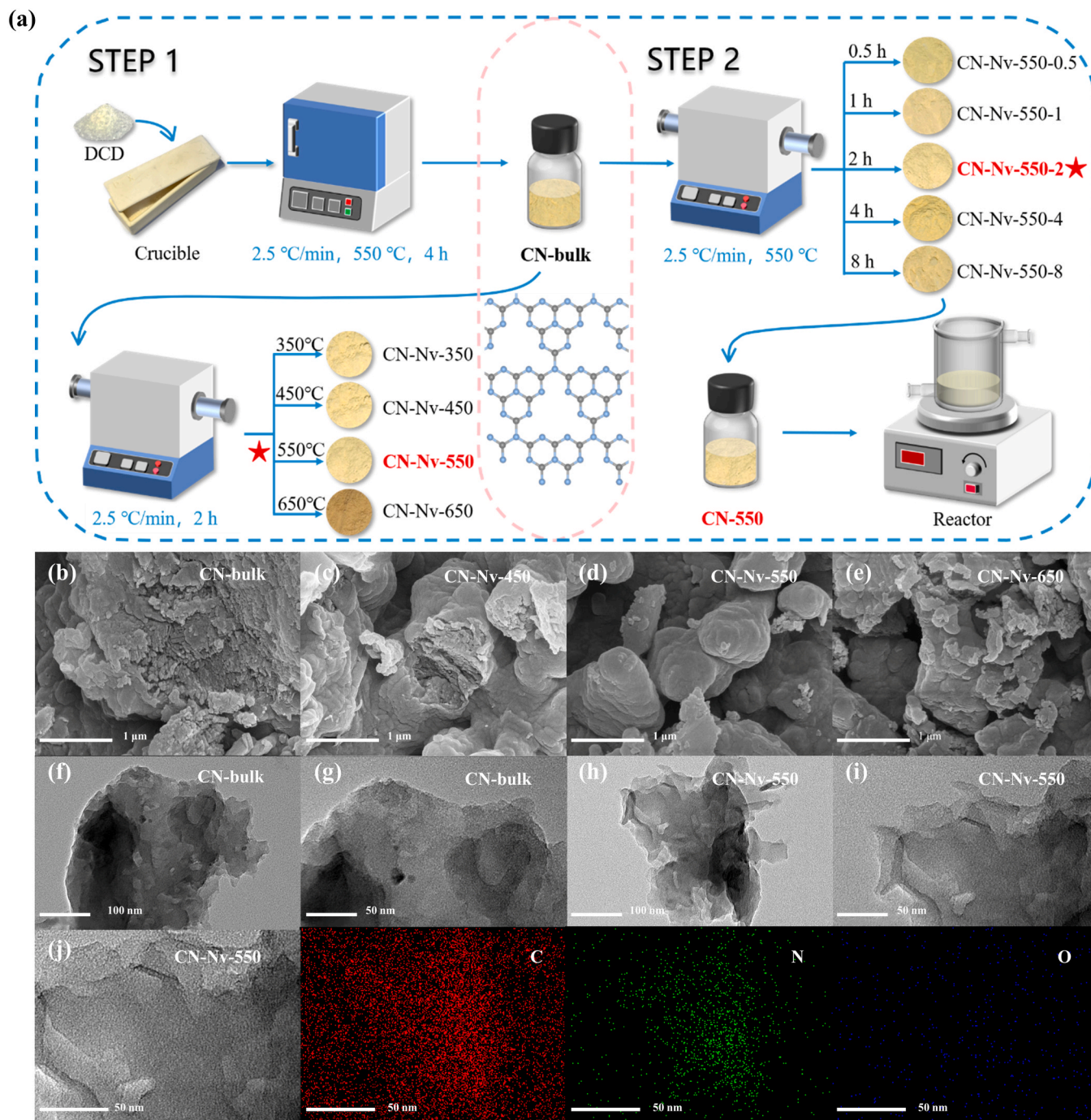

Fig. 2. Synthesis of Nv-rich g-C$_3$N$_4$ and validation of morphology. a, Schematic diagram of CN-550 synthesis. b-e, SEM images of (b) CN-bulk, (c) CN-Nv-450, (d) CN-Nv-550, and (e) CN-Nv-650. f-i, TEM images of (f-g) CN-bulk, (h-i) CN-Nv-550. j, TEM elemental mappings of CN-Nv-550.

E_{tot}, E_s, and E_m depict the total energies of the adsorption configuration, the catalyst samples, and the isolated molecule, respectively.

3. Results and discussion

3.1. Predicting the intrinsic properties of catalysts

First, we conducted theoretical calculations to investigate the impact of nitrogen vacancies (Nv) on the intrinsic properties of g-C$_3$N$_4$ and their potential for oxidant activation. The charge properties of g-C$_3$N$_4$ were investigated using density of states (DOS) calculations. As shown in

Fig. 1a, b, the valence band (VB) and conduction band (CB) of CN-bulk and CN-550 were mainly contributed by N and C elements, respectively. The introduction of Nv resulted in a narrowing of the catalyst band gap, indicating enhanced visible light absorption in g-C$_3$N$_4$. Notably, a small defective energy level near the Fermi level was observed in the CN-550 diagram (Fig. 1b), indicating that Nv facilitated the internal electron transfer within the material.

Immediately after, we calculated the work functions to evaluate the minimum energy required for electron transfer from the Fermi energy level to the vacuum level. The calculated results (Fig. 1c, d) show that the work functions of CN-bulk and CN-550 were 6.52 eV and 5.22 eV,
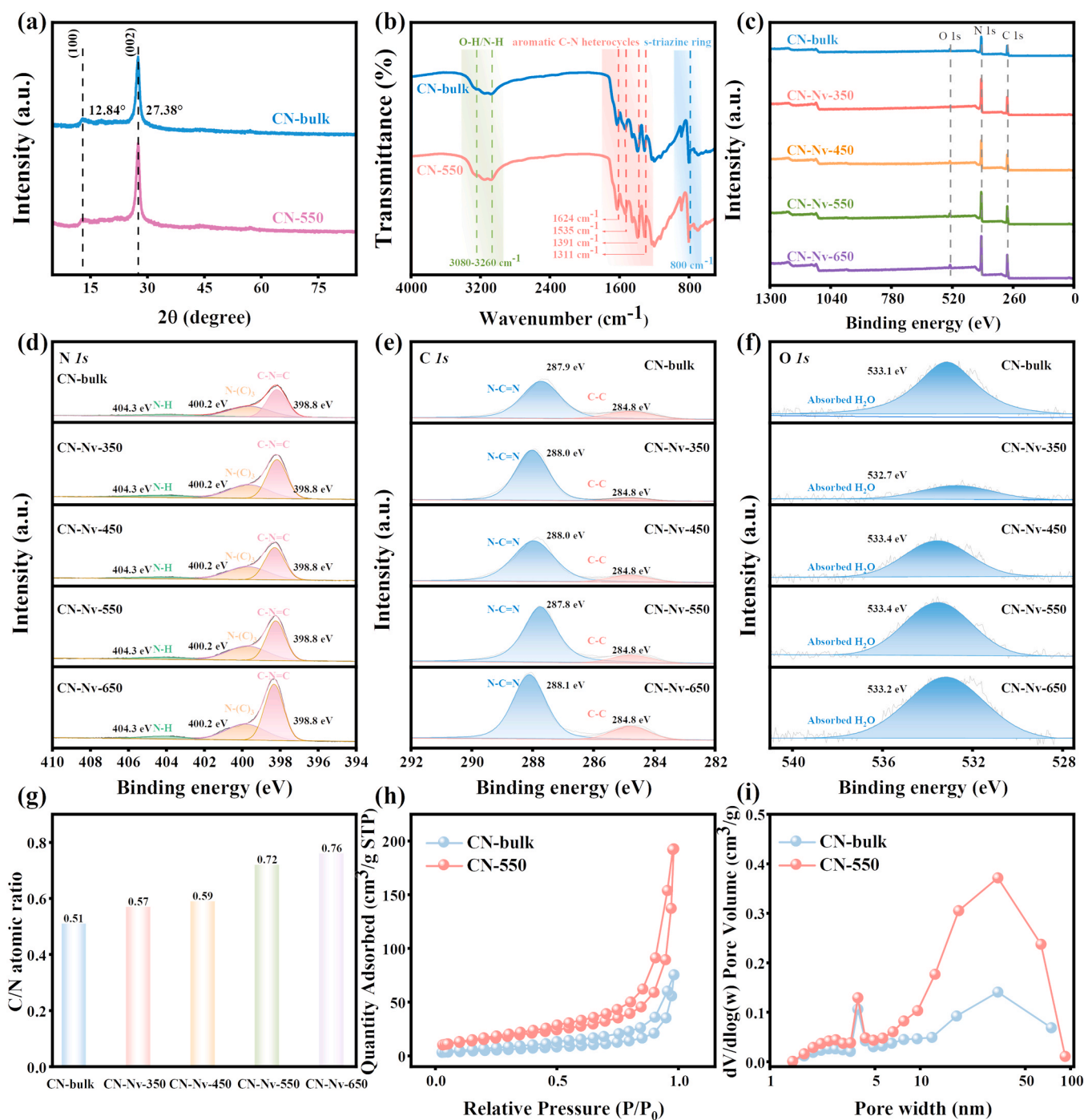

Fig. 3. Characterization of Nv-rich g-C$_3$N$_4$. XRD patterns (a) and FTIR spectra of different catalysts (b). c, d, e, f, XPS spectra comparisons: (c) Survey, (d) N 1 s, (e) C 1 s, and (f) O 1 s of different catalysts. g, C/N atomic ratio in different catalysts. h, N$_2$ adsorption-desorption isotherms of different prepared catalysts. i, The corresponding pore size distribution of CN-bulk and CN-550.

respectively. This suggests that Nv reduced the potential energy barrier for electron escape from the g-C$_3$N$_4$ material to the vacuum, thereby improving the photocatalytic performance of Nv-containing materials.

Meanwhile, the two-dimensional electron density maps of CN-bulk and CN-550 are presented in Fig. 1e, f. The CN-bulk exhibited a highly symmetric electron distribution, while the introduction of Nv resulted in a pronounced redistribution of electrons. This electron redistribution facilitated subsequent electron transfer during the subsequent periodate (PI) activation.

Overall, the theoretical calculations confirmed that incorporating Nv into the CN-bulk framework enhanced visible light absorption and significantly promoted charge transfer. This indicated that the involvement of Nv was a more desirable choice for the visible-light-assisted activation of PI.

3.2. Characterization of different catalysts

Based on the aforementioned results, as illustrated in Fig. 2a, we designed a straightforward method to introduce Nv into CN-bulk by subjecting it to secondary N$_2$ atmosphere calcination at various temperatures. Scanning electron microscopy (SEM) was used to analyze the catalyst's morphologies. As depicted in Fig. 2b-e, CN-bulk exhibited a bulk structure that transformed into nanosheets as the initial calcination temperature increased. This observation was further supported by transmission electron microscopy (TEM) images (Fig. 2f-i). Additionally, TEM-EDS mapping was employed to examine the elements present in CN-550 (Fig. 2j), revealing that C, N, and O elements were uniformly distributed throughout the g-C$_3$N$_4$ framework.

X-ray diffraction (XRD) patterns analyzed the different samples' structures (Fig. 3a). Both CN-bulk and CN-550 contained similar two characteristic peaks (12.84° and 27.38°), attributable to the in-plane packed heptazine units (100) and π–π interlayer stacking (002) of g-C$_3$N$_4$ [39,40]. The involvement of Nv did not affect the g-C$_3$N$_4$'s structure but favored its property modulation. Fourier Transform Infrared Spectroscopy (FTIR) identified more chemical structural properties. Similar to the XRD results, the profiles of CN-bulk and CN-550 displayed minimal differences (Fig. 3b). The characteristic peaks at 800 cm^{-1} were assigned to the out-of-plane bending mode of heptazine rings of g-C$_3$N$_4$ [41]. Several peaks in the 1200–1650 cm^{-1} corresponded to the stretching vibration modes of aromatic heterocycles in the g-C$_3$N$_4$ framework [42]. Furthermore, the characteristic peaks in 3080–3260 cm^{-1} belonged to the O-H or N-H stretching vibration peaks [43].

X-ray photoelectron spectroscopy (XPS) analysis was used to investigate different materials' chemical states and compositions. In the survey spectra, the main elemental compositions are C, N, and O, in agreement with the TEM-mapping results (Fig. 3c). In N 1 s spectra (Fig. 3d, Table S2), the characteristic peaks at 398.8, 400.2, and 404.3 eV belonged to sp^2-hybridized nitrogen (C-N = C), tertiary nitrogen (N-C$_3$), and terminal amino groups (N-H), respectively [34]. The different catalysts in C 1 s profiles (Fig. 3e, Table S3) contained two characteristic peaks, 284.8 and 288.0 eV, corresponding to the C-C groups (C impurity) and sp^2-hybridized carbon (N-C=N), respectively [31]. For the O 1 s spectra (Fig. 3f, Table S3), a characteristic peak, 533.1 eV, was attributed to the adsorbed H$_2$O [44]. To further illustrate the formation of Nv and its concentration modulation by secondary calcination at different temperatures, we compared the C/N ratios of different materials (Fig. 3g, Table S4). The results show that the C/N ratios increased with temperature, indicating successful Nv formation that increased with calcination temperature (from 0.57 at 350 °C to 0.76 at 650 °C). Moreover, the Nv was analyzed using solid-state electron spin resonance (ESR, Fig. S1), revealing an enhanced Nv signal compared to CN-bulk and thus confirming successful Nv insertion.

Furthermore, we investigated the potential impact of Nv introduction on the reaction's specific surface area. The results show that CN-bulk and CN-550 exhibited a classical IV isotherm and similar

mesopore distribution (Fig. 3h, Table S5), with the specific surface area increasing from 22.41 to 62.72 m^2·g^{-1}. The pore volume was also increased due to the intervention of Nv (Fig. 3i, Table S5), which favored the subsequent catalytic reaction.

The photocatalytic performance of a material is greatly influenced by its light-harvesting ability, carrier separation, and charge transfer capabilities [45]. Thus, UV–visible diffuse reflectance spectra (UV–vis DRS) were initially employed to compare light absorption properties (Fig. 4a). The absorption wavelength of CN-550 exhibited an increase compared to that of CN-bulk, and the corresponding bandgap decreased from 2.72 to 2.68 eV. These findings suggest that introducing Nv enhances visible light absorption and promotes the generation of additional charge carriers. To further investigate the separation and transfer kinetics of photogenerated carriers, photoluminescence spectroscopy (PL) was performed with excitation at 350 nm (Fig. 4b). The PL intensity of CN-550 was significantly lower than that of CN-bulk, indicating suppressed carrier recombination and accelerated internal charge separation in the presence of Nv.

Photoelectric tests were then conducted to compare the photoelectrochemical properties of the as-prepared catalysts. The results revealed that CN-550 exhibited a higher photocurrent (Fig. 4c) and a smaller electrochemical impedance circular arc (Fig. 4d), indicating that the introduction of Nv into g-C$_3$N$_4$ reduced the internal charge transfer resistance and enhanced the kinetics of carrier separation.

These findings suggest that Nv played a crucial role in enhancing light absorption and facilitating efficient charge separation, leading to the generation and utilization of more active carriers in the subsequent reaction.

3.3. Catalytic performance evaluation in the constructed CN-550/PI/vis system

Bisphenol A (BPA), a typical endocrine disruptor, was selected as the target contaminant to evaluate the catalytic performance of the constructed system. As shown in Fig. 5a (Table S6), the PI/vis alone and CN-550/PI/dark systems exhibited negligible catalytic performance, indicating that visible light alone was unable to directly activate PI, and no degradation of the pollutant occurred in the absence of light. In addition, CN-550 alone achieved only approximately 20.4% BPA removal under visible light, indicating that photocatalysis alone was insufficient for effective degradation. However, the combination of PI, CN-550, and visible light led to the complete removal of BPA within 30 min, with a reaction rate constant of 8.06×10^{-2} min^{-1}, which was 38.38 and 9.37 times higher than that of PI/vis and CN-550/vis systems, respectively. In contrast, the reaction rate constant of the CN-550/PI/dark system was nearly zero. These results demonstrate that introducing Nv into g-C$_3$N$_4$ enabled effective activation of PI under visible-light-assisted conditions.

Different Nv concentrations were introduced into CN-bulk by varying the calcination temperatures. As shown in Fig. 5b (Table S7), at 350 °C, Nv had not yet formed, and the catalytic performance was similar to that of the CN-bulk/PI/vis system. When the calcination temperature was raised to 450 °C, a small amount of Nv began to be formed, thus promoting the catalytic reaction. At 550 °C, the optimal Nv production was achieved, resulting in the highest activity. However, excessive Nv formation occurred at higher temperatures, decreasing reaction kinetics. Thus, the concentration of Nv acted as a double-edged sword that required careful management to achieve optimal catalytic performance.

Furthermore, the influence of calcination duration was investigated (Fig. 5c, Table S7). The results show that the maximum reactivity could be achieved with a secondary calcination duration of 2 h. Prolonging the time beyond this point had a detrimental effect on the performance. Therefore, for the sake of practicality and efficiency, two hours was determined as the most suitable for subsequent material synthesis. The amount of CN-550 catalyst also significantly impacted BPA removal (Fig. 5d). When using 0.1 g/L of the catalyst, only 51.0% removal of BPA
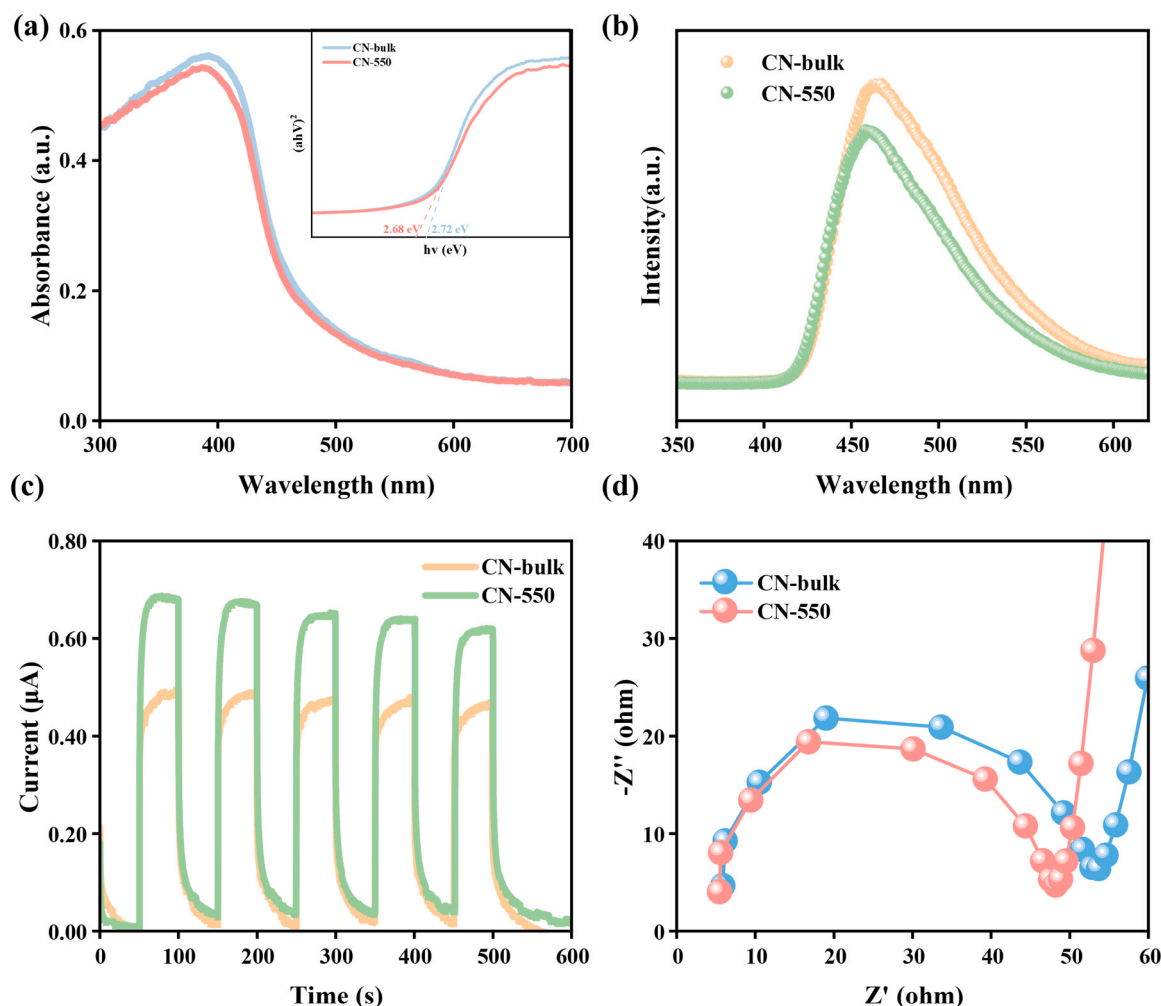
Fig. 4. Light-harvesting capability of the catalyst and the corresponding carrier separation and charge transfer ability. a, UV–vis DRS. b, PL. c, i-t. d, EIS.

was achieved. While the catalytic performance continued to improve with the increased amounts of CN-550, factors such as cost investment and the ease of studying reaction kinetics were considered. As a result, a dosing amount of 0.2 g/L was selected for subsequent experiments. Moreover, as depicted in Text S4, it was observed that the optimum values for all photocatalysts fell within the range of 0.2–0.3 g/L. Interestingly, this range aligned perfectly with the reactor's optimal optical thickness values (1.8–4.4), which agreed with the experimental results. These findings indicate a clear correlation between photocatalyst concentration, optical thickness, and the performance of the catalytic system. By maintaining the catalyst concentration within this optimal range, we could achieve the desired optical thickness and maximize the efficiency of the photocatalytic reaction. This understanding allowed for the precise control and optimization of the photocatalytic process, ensuring optimal performance and effectiveness in practical applications.

The amount of PI also played a crucial role in the CN-550/PI/vis system. Fig. 5e (Table S8) shows that with a PI concentration of 0.01 mM, the BPA removal was only 24.7%. As the PI amount increased from 0.01 to 1 mM, BPA removal efficiency reached 100%, and the kinetic constant rose from 1.09×10^{-2} to 8.06×10^{-2} min^{-1}. However, when the amount of PI increased to 2 mM, the kinetic constant decreased slightly to 8.03×10^{-2} min^{-1}. The addition of excess PI to the system might lead to competition between PI and BPA, as well as its intermediates, for reactive free radicals. The results suggest that within a suitable range, increasing the concentration of PI could effectively utilize the photogenerated electrons in the photocatalytic system, thereby

enhancing its intrinsic performance. Concurrently, PI could be activated after accepting electrons to produce more active species and accelerate the reaction. We selected 1 mM of PI as the optimal injection amount for subsequent degradation reactions.

Furthermore, the performance of the CN-550/PI/Vis system exhibited a distinct trend with different BPA concentrations (Fig. 5f, Table S8). The system demonstrated rapid degradation of BPA at low concentrations of 10 mg/L. However, the catalytic performance significantly decreased as the BPA concentration increased to 20 mg/L. This result could be attributed to two main reasons: firstly, a higher BPA concentration limits the exposure of active sites during the reaction. Secondly, more intermediates were generated, which competed for the limited adsorption and catalytic sites throughout the reaction process [46]. In real wastewater scenarios, BPA was typically detected at concentrations below 10 mg/L, indicating that the CN-550/PI/vis system possesses a distinct advantage in decontamination capabilities.

To verify the function of Nv, we simultaneously selected three oxidants commonly used in reported systems [47], hydrogen peroxide (H$_2$O$_2$), peroxymonosulfate (PMS), and peroxydisulfate (PDS) (Fig. 6a, Table S9). The results revealed that CN-550 exhibited superior activation potential for asymmetrical oxidants, particularly PMS. Notably, among the four oxidants compared, the CN-550/PI/vis system in this study demonstrated the optimal catalytic performance, highlighting its potential for practical applications. Furthermore, we compared our system to previously reported systems for BPA removal. The CN-550/PI/vis system exhibited superior activity, advantages in reaction kinetics, and a simple, scalable production method (Fig. 6b,
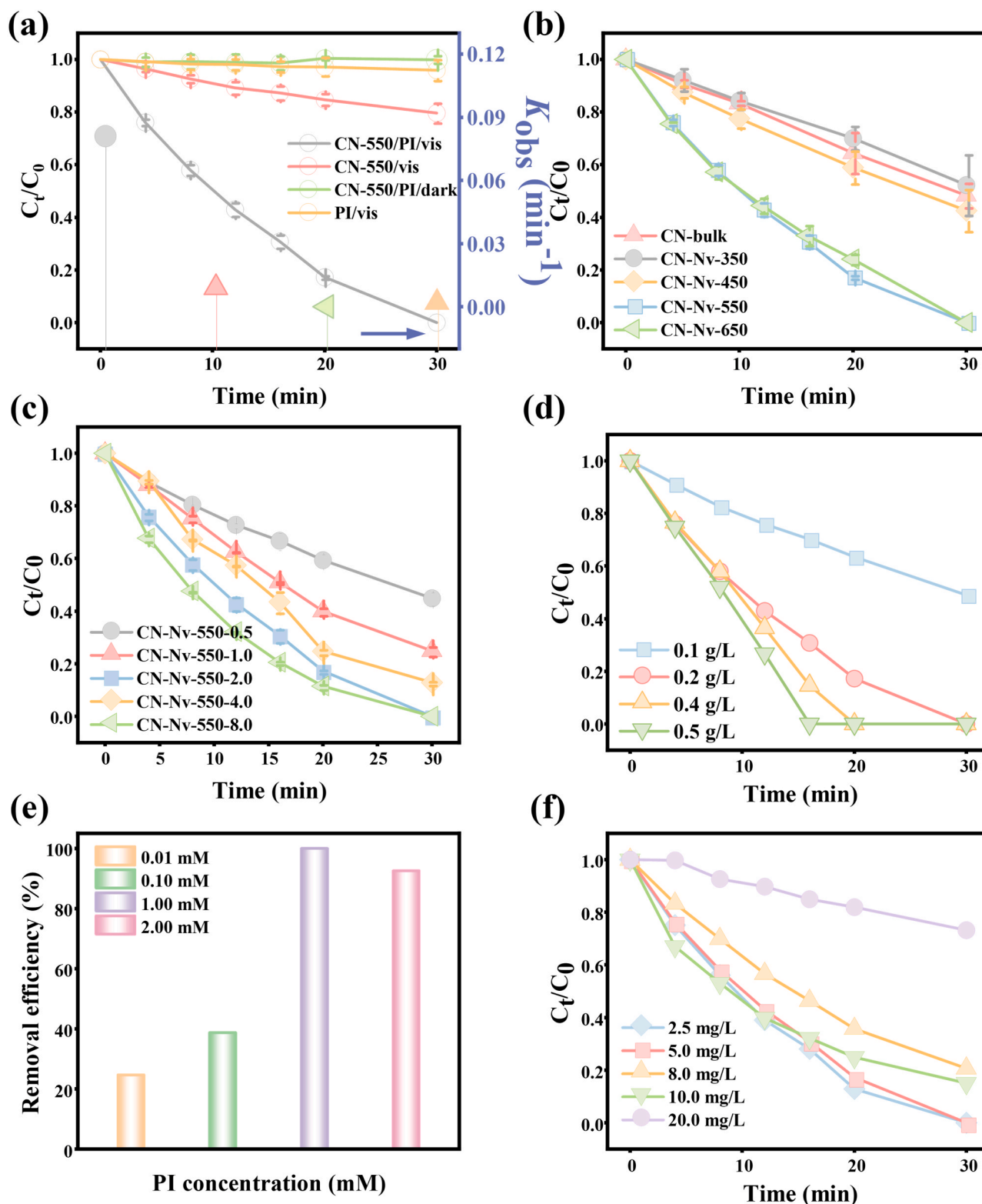
Fig. 5. Optimization and evaluation of CN-550/PI/vis system. a, Degradation of BPA in different catalytic systems. b, Degradation of BPA by materials with different temperatures. c, Degradation of BPA by materials with different calcination times. Degradation of BPA using CN-550/PI/vis system at different (d) CN-550 dosages, (e) PI concentrations, and (f) BPA concentrations.

Table S10-1). This system's kinetic coefficient of activity also outperformed those of the previously reported systems. These findings further validate the efficiency and applicability of the CN-550/PI/vis system for BPA removal.

In addition to evaluating the pollutant removal, we also assessed the mineralization degree, the toxicity of the formed intermediates, and potential removal pathways. Compared to the CN-bulk/PI/vis system, the CN-550/PI/vis system exhibited an increase in the mineralization of BPA from 0% to 51.68% (Fig. S2), indicating simultaneous degradation and mineralization processes. LC-MS analyses identified the main
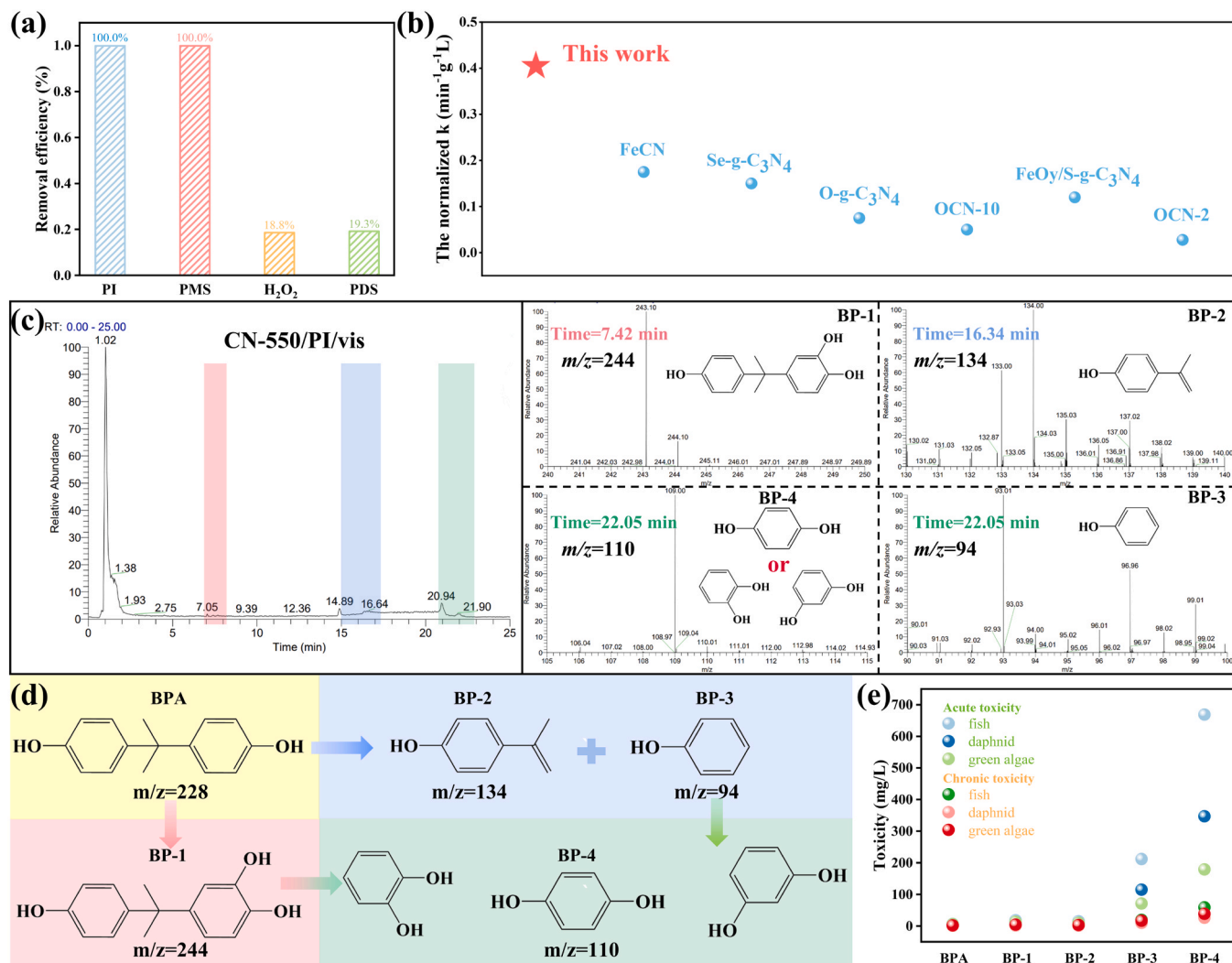
Fig. 6. BPA intermediates and removal pathways. a, Degradation of BPA in the presence of different oxidants. b, Comparison of the normalized k of different reported works. c, The intermediates of BPA degradation. d, Degradation pathways of BPA. e, Possible changes in toxicity of different products.

aromatic intermediates formed during BPA degradation, including phenol, 4-isopropylphenol, 2-hydroxy-bisphenol A, hydroquinone, resorcinol, and catechol (Fig. 6c, Table S10-2). Based on these results and previous studies, we proposed potential degradation pathways of BPA by activating PI over the CN-550 catalyst (Fig. 6d). On the one hand, the BPA molecule underwent attack by radicals, leading to its transformation into phenol and 4-isopropylphenol. On the other hand, hydroxylation of BPA resulted in the formation of 2-hydroxy-bisphenol A. Furthermore, phenol was oxidized to three types of dihydroxy benzenes through hydroxylation of the aromatic ring in the para/ortho/meta positions. Additionally, the toxicity of the degradation products was assessed using Ecological Structure-Activity Relationships models (ECOSAR) (Fig. 6e, Table S11). The results showed a significant decrease in toxicity compared to the original BPA, indicating a detoxification during the PI activation. These findings demonstrate the potential of the constructed CN-550/PI/vis system for decontaminating organic wastewater.

3.4. Reveal the intrinsic reaction mechanism in the CN-550/PI/vis system

To identify the dominant active species in the CN-bulk/PI/vis and CN-550/PI/vis systems, we conducted a quenching experiment using various trapping agents (Fig. 7a, b, Table S12). Here, TBA, EDTA-2Na, BQ, and *L*-Histidine were used as trapping agents [48] for hydroxyl

radicals ($^{\bullet}OH$), the photo-induced holes (h^+), superoxide anions radicals ($^{\bullet}O_2^-$), and singlet oxygen ($^1O_2$), respectively. These trapping agents were individually added to the catalytic system to determine their specific roles in the reaction. In contrast to the CN-bulk/PI/vis system, where the primary active species were $^{\bullet}O_2^-$, $^1O_2$, and $^{\bullet}OH$, the CN-550/PI/vis system primarily generated $^{\bullet}O_2^-$, $^1O_2$ and $^{\bullet}OH$ as the main active species. Additionally, the photo-induced h^+ acted as an auxiliary species in the CN-550/PI/vis system. This observation suggests that the accumulated h^+ species could exert their oxidation capacity once the electrons were efficiently transferred to PI.

The electron spin resonance (ESR) technique was employed further to confirm the role of the corresponding active species. As shown in Fig. 7c, it can be observed that CN-550 generated a higher amount of photo-induced holes (h^+) compared to CN-bulk, and the utilization of h^+ was enhanced with the addition of BPA. This finding indicates that introducing Nv increased the number of carriers, thereby improving the oxidation performance of the remaining h^+ after rapid electron transfer. In the DMPO-$^{\bullet}O_2^-$ patterns (Fig. 7d), $^{\bullet}O_2^-$ yield of CN-bulk and CN-550 were similar, suggesting that the photogenerated electrons generated by introducing Nv partly directly participated in the activation of molecular oxygen. The other portion of electrons effectively transferred to activated PI, contributing to the activation reaction and generating more active species. Similarly, the DMPO-$^{\bullet}OH$ signals showed a similar trend (Fig. 7e), indicating a consistent molecular oxygen activation. In the ESR
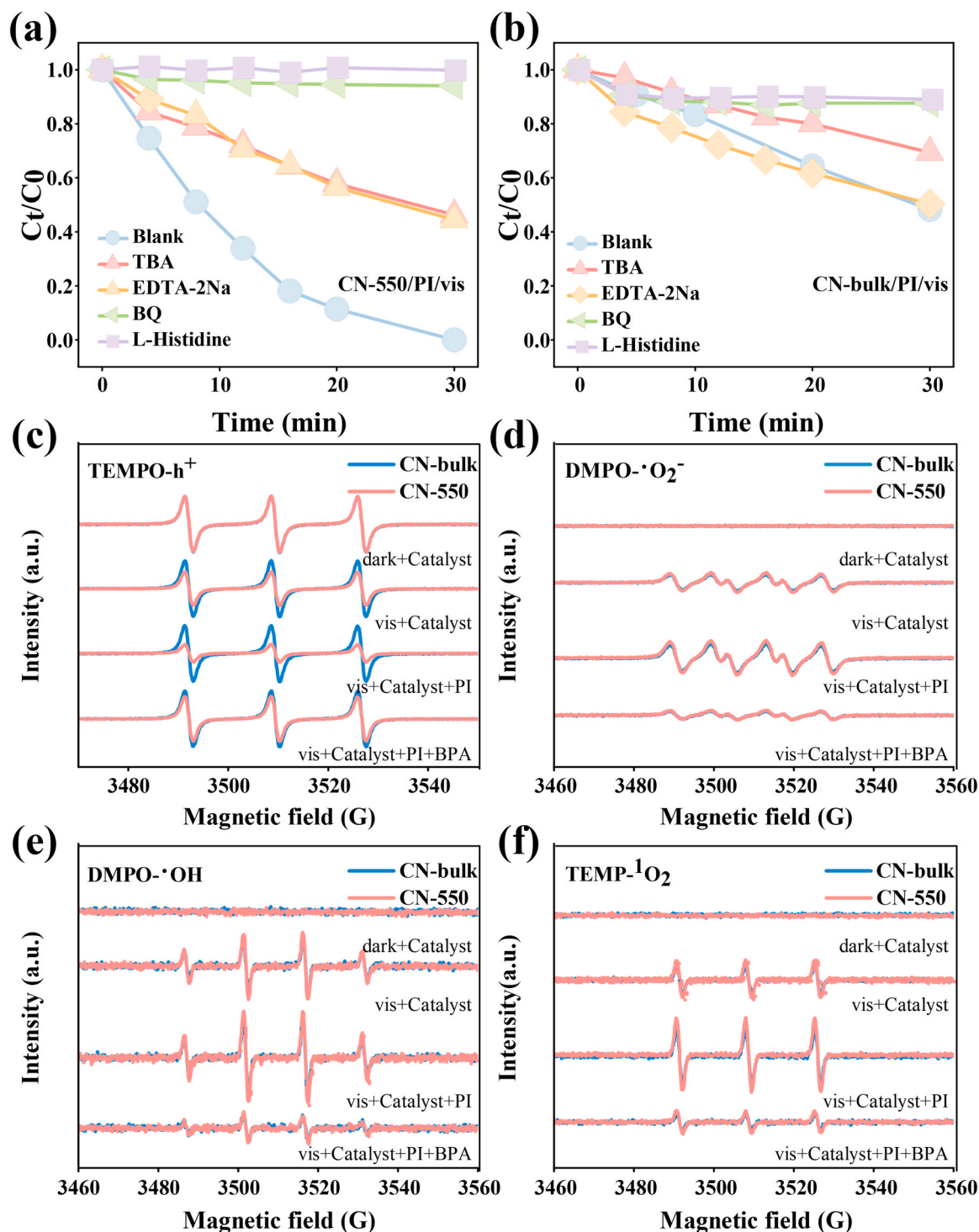
Fig. 7. Identification of the key reactive species. a, b, Degradation of BPA in the presence of various scavengers in the (a) CN-550/PI/vis, (b) CN-bulk/PI/vis systems, respectively. c, d, e, f, Comparison of ESR signals between CN-bulk/PI/vis and CN-550/PI/vis systems: (c) TEMPO-h$^+$, (d) DMPO-$^\bullet$O$_2^-$, (e) DMPO-$^\bullet$OH and (f) TEMP-^{1}O$_2$.

results of ^{1}O$_2$ (Fig. 7f), more ^{1}O$_2$ was produced in the CN-550/PI/vis system, suggesting that ^{1}O$_2$ was also generated in the PI activation system in addition to the molecular oxygen pathway.

Also, we identified the highly active species produced during the PI activation. Based on previous reports, we also investigated the potential formation of iodine-active species. The generation of IO$_3^\bullet$ in the CN-550/PI/vis system was determined by comparing the yield of IO$_3^-$ before and after the addition of 4-CP. The obtained result (Fig. S3, Text S1)

confirmed the production of IO$_3^\bullet$ species in the CN-550/PI/vis system), contributing to the rapid decontamination during the catalytic reaction.

Although PI itself is non-toxic, the possible formation of iodine species such as HOI, I$_2$, or I$_3^-$ during the PI-based AOPs can be bactericidal and may lead to the production of undesired iodinated disinfection by-products (DBPs) when reacting with natural organic substances. Thus, such validation should be conducted. Excitingly, the experimental evidence presented in Figs. S4 and S5 (Text S2) confirmed the absence of

HOI, I_2, or I_3 in the constructed CN-550/PI/vis system, ruling out the formation of potential iodine by-products. This indicates that the CN-550/PI/vis system has great potential for the purification of organic wastewater without the formation of undesired iodinated DBPs.

To gain a deeper understanding of the intrinsic catalytic mechanism of the CN-550/PI/vis system, we conducted theoretical calculations. We obtained insights into the possible mechanism by analyzing small molecules' adsorption and charge density differences, such as BPA and PI. Using density functional theory (DFT), we first calculated the surface adsorption of CN-bulk and CN-550 materials on BPA (Fig. 8a, Table S13). The adsorption energies were − 0.11 eV and − 0.16 eV for CN-bulk and CN-550, respectively. This indicates that BPA had a higher affinity for adsorption onto the CN-550 surface. Furthermore, we calculated the charge density difference between BPA and the catalyst. Fig. 8b shows a more significant electron transfer between BPA and CN-550, suggesting that BPA, an electron-rich pollutant, could readily donate electrons, accelerating the reaction process.

To investigate the adsorption of the catalyst and PI, we calculated the adsorption energy by determining the difference in conformational energy (E_{tot}) before and after adsorption. By controlling the distance between PI and catalyst surface and simulating the process of PI adsorption, we obtained the adsorption energies of CN-bulk and CN-550, and PI to be −1.96 eV and −3.22 eV, respectively (Fig. 8c, Fig. S6 and Table S13). These results indicate that PI had a stronger affinity for
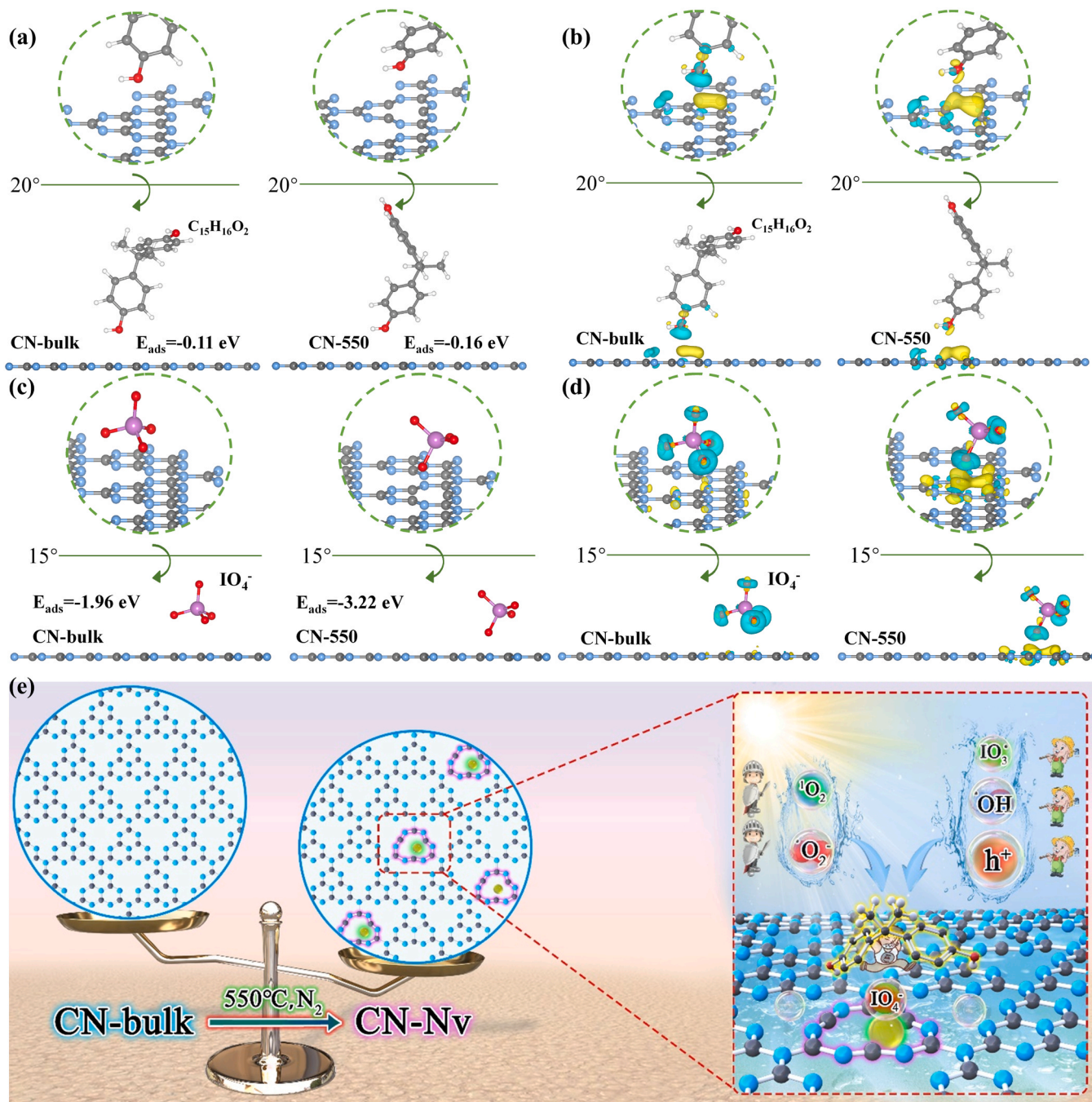

Fig. 8. DFT calculations. a, The adsorption configurations of BPA on CN-bulk and CN-550. b, The differential charge density of adsorbed BPA with CN-bulk and CN-550. c, The adsorption configurations of IO_4 on CN-bulk and CN-550. d, The differential charge density of adsorbed IO_4 with CN-bulk and CN-550. e, A possible photocatalytic mechanism for visible-light-assisted PI activation using CN-550.

adsorption onto the CN-550 surface. Additionally, we calculated the charge density difference between PI and catalysts (Fig. 8d). The analysis of electron cloud distribution on the contaminant's surface and the catalyst surface revealed a greater transfer of electrons between PI and CN-550. This indicates that the presence of Nv served as a continuous and significant source of electron input to the oxidant, leading to increased activation of PI and the generation of more active species.

The results demonstrate that introducing Nv significantly enhanced the adsorption of substances in the reaction and promotes electron transfer between BPA, PI, and CN-550. This enhanced electron transfer facilitated the rapid activation of PI and promoted decontamination. The mechanism diagram of the CN-550/PI/vis system for the efficient removal of organic pollutants is depicted in Fig. 8e. With the introduction of Nv, an increased production of carriers, particularly photo-generated electrons, occurs. These electrons can effectively transfer to PI, generating highly oxidative species such as $IO_3^{\bullet}$, $^{\bullet}O_2^{-}$, $^1O_2$, $^{\bullet}OH$, and h^+. Additionally, the rapid transfer of photogenerated electrons enhances the oxidation performance of accumulated holes (h^+) in the valence band (VB). The activation of PI was significantly enhanced

under visible light, acting as a switch to accelerate decontamination process. Furthermore, the introduction of Nv promoted an in-situ adsorption and activation of reaction medium, thereby enhancing the overall removal capacity.

3.5. Feasibility and stability of the CN-550/PI/vis system

To evaluate the system's practical applicability, we conducted tests to examine its resistance to environmental factors. Firstly, we investigated the pH effect on the CN-550/PI/vis system and observed that it exhibited the highest activity under near-neutral conditions (Fig. 9a, Table S14). Remarkably, it also displayed good activity (~86.7%), even under strongly acidic and basic conditions, surpassing the pH dependence observed in conventional transition-metal-based systems. Secondly, we examined the influence of natural organic matter, specifically humic acid (HA). The role of HA was found to be both beneficial and detrimental. HA competed for active sites at low concentrations (5–20 mg/L), resulting in reduced BPA removal. However, at a concentration of 40 mg/L, the activity of the CN-550/PI/vis system
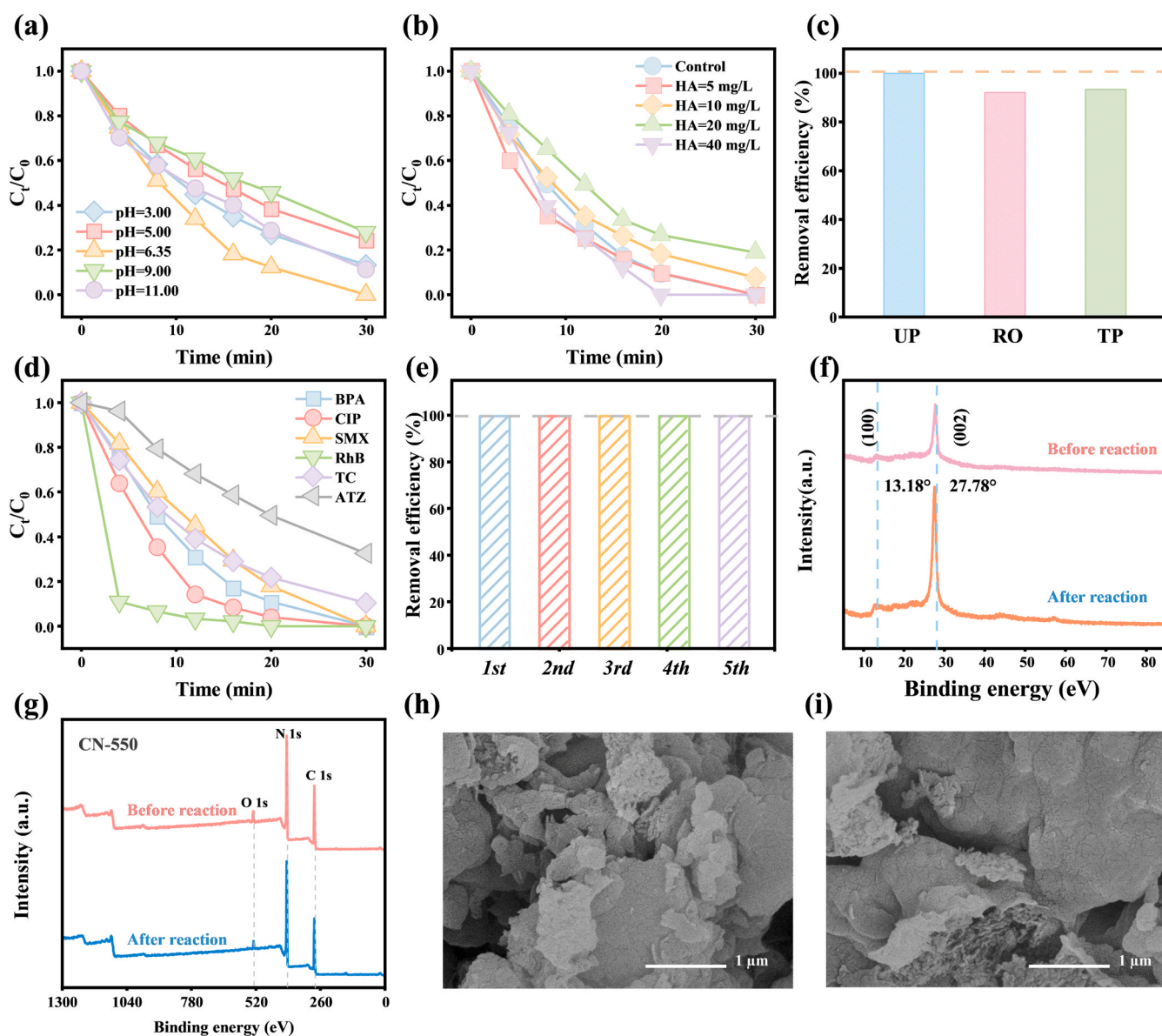

Fig. 9. Feasibility and stability of the CN-550/PI/vis system. Effects of a, pH. b, Different HA doses. c, Various water resources. d, Degradation of various organic pollutants. e, Stability test of CN-550. f-i, Characterization of CN-550 after the reaction. f, XRD patterns. g, XPS spectra. h-i, SEM images.

exhibited a noticeable increase, likely attributed to the reducing components of HA, such as quinones (Fig. 9b, Table S15). Thirdly, we investigated the impact of coexisting ions (Fig. S7). The presence of most conventional ions had insignificant effects on BPA removal, except for CO_3^{2-} and NO_2^-, which could either convert highly reactive species or consume oxidants [5,49]. Additionally, we examined the system's performance using different water sources, including deionized water, tap water, and reverse osmosis water and found a slight variation in BPA removal efficiency (Fig. 9c, Table S16). Lastly, the CN-550/PI/vis system demonstrated a broad spectrum of effectiveness against various organic contaminants (Fig. 9d, Table S17). These findings further confirm the CN-550/PI/vis system's potential for practical applications. Notably, the PI utilization in the current system (Fig. S8) was only 10.12%. Further studies can be focused on investigating methods to enhance PI utilization and maximize the catalytic performance of the CN-550/PI/vis system.

Moreover, the cycling stability of the CN-550/PI/vis system was explored (Fig. 9e). Remarkably, the system maintained a 100% BPA removal efficiency even after five consecutive experiments, demonstrating its excellent stability for continuous use. To further assess the catalyst's stability, the used catalysts were collected and analyzed using XRD (Fig. 9f), XPS (Fig. 9g), and SEM (Fig. 9h, i). The catalyst, CN-550, exhibited excellent recyclability, as no significant changes were observed in its structure, composition, or morphology before and after the reaction. This finding further confirms the stability and recyclability of CN-550, making it a promising catalyst for repeated use in practical applications. To further investigate the stability of CN-550, we also evaluated its performance under various pH conditions, mimicking real wastewater scenarios. The collected CN-550 samples, after different pH reactions, were subjected to SEM and FTIR characterization. The SEM analysis (Fig. S9) and FTIR spectra (Fig. S10) revealed that CN-550 remained unchanged despite harsh pH conditions. These findings suggest that the CN-550 exhibited excellent stability, highlighting its potential for practical applications in wastewater treatment.

4. Conclusions

In this study, we utilized a secondary N_2 calcination to introduce Nv into the g-C_3N_4 framework, resulting in an efficient photo activator for PI activation. Such a catalytic system demonstrated rapid degradation of the target pollutant BPA, achieving complete removal with a 100% efficiency. Compared to the monomer CN-bulk/PI/vis, the reaction kinetics of the CN-550/PI/vis system were improved by 3.36-fold. This constructed system exhibited remarkable capability in eliminating various organic pollutants, even under complex ion coexistence and variable pH conditions. The mineralization efficiency of BPA was enhanced from 0% to 51.68%, and the system maintained its high removal efficiency over five consecutive cycles. Through capture experiments, probes, ESR, and theoretical calculations, we observed that suitable Nv concentrations significantly enhanced the activation of oxidants, leading to the generation of highly active species such as IO_3^-, $^{\bullet}O_2^-$, $^1O_2$, $^{\bullet}OH$, and h^+. Moreover, by utilizing PI as an electron acceptor, the oxidation capacity of accumulated holes in the valence band was significantly amplified. We thoroughly investigated the potential removal pathways of BPA and the evolution of by-product toxicity. Through our comprehensive analysis, we gained valuable insights into designing highly efficient and eco-friendly systems for oxidant activation, particularly shedding light on the underlying catalytic mechanisms of PI activation. This study contributes significantly to the advancement of knowledge in this field and provides important information for the development of effective and environmentally friendly oxidant activation systems.

CRediT authorship contribution statement

Fei Chen conceived and planned the experiments, and Zhuo-Ya Fang

and Yi-Jiao Sun performed the related experiments. Xin-Tong Huang contributed to the DFT calculation. Fei Chen, Zhuo-Ya Fang, and Yi-Jiao Sun conducted, and Chang-Wei Bai, Ke-An Zhu, Xin-Jia Chen, Bin-Bin Zhang, Yi-Shuo Zhang, Qi Yang, and Jie-Xuan Zheng assisted in collecting data and analyzing various characterizations. Zhuo-Ya Fang, Yi-Jiao Sun, and Fei Chen wrote and revised the manuscript.

Declaration of Competing Interest

The authors declare that they have no known competing financial interests or personal relationships that could have appeared to influence the work reported in this paper.

Data Availability

Data will be made available on request.

Acknowledgments

Appendix A. Supporting information

Supplementary data associated with this article can be found in the online version at doi:10.1016/j.apcatb.2023.122994.

References

[1] Y. Shang, X. Xu, B. Gao, S. Wang, X. Duan, Single-atom catalysis in advanced oxidation processes for environmental remediation, Chem. Soc. Rev. 50 (2021) 5281–5322.

[2] J. Xiao, Y. Xie, J. Rabeah, A. Bruckner, H. Cao, Visible-light photocatalytic ozonation using graphitic C_3N_4 catalysts: a hydroxyl radical manufacturer for wastewater treatment, Acc. Chem. Res. 53 (2020) 1024–1033.

[3] S. Li, Y. Liu, Y. Wu, J.R. Hu, Y.Q. Zhang, Q. Sun, W.L. Sun, J.G. Geng, X.Y. Liu, D. T. Jia, X.Q. You, D.Q. Qi, M.R. Tang, Y.T. Lyu, F.G. Kong, L.L. Cai, Y.F. Ai, Y. C. Wang, J.R. Ni, Antibiotics in global rivers, Nation Sci. Open 1 (2022), 20220029.

[4] Z. Wang, A. Berbille, Y. Feng, S. Li, L. Zhu, W. Tang, Z.L. Wang, Contact-electro-catalysis for the degradation of organic pollutants using pristine dielectric powders, Nat. Commun. 13 (2022) 130.

[5] X. Duan, H. Sun, S. Wang, Metal-free carbocatalysis in advanced oxidation reactions, Acc. Chem. Res. 51 (2018) 678–687.

[6] H. Sun, F. He, W. Choi, Production of reactive oxygen species by the reaction of periodate and hydroxylamine for rapid removal of organic pollutants and waterborne bacteria, Environ. Sci. Technol. 54 (2020) 6427–6437.

[7] Y. Kim, H. Lee, H. Oh, Z. Haider, J. Choi, Y.U. Shin, H.I. Kim, J. Lee, Revisiting the oxidizing capacity of the Periodate-H_2O_2 mixture: identification of the primary oxidants and their formation mechanisms, Environ. Sci. Technol. 56 (2022) 5763–5774.

[8] A.D. Bokare, W. Choi, Singlet-Oxygen generation in alkaline periodate solution, Environ. Sci. Technol. 49 (2015) 14392–14400.

[9] Y. Long, J. Dai, S. Zhao, Y. Su, Z. Wang, Z. Zhang, Atomically dispersed cobalt sites on graphene as efficient periodate activators for selective organic pollutant degradation, Environ. Sci. Technol. 55 (2021) 5357–5370.

[10] Y. Long, J. Dai, S. Zhao, S. Huang, Z. Zhang, Metal-organic framework-derived magnetic carbon for efficient decontamination of organic pollutants via periodate activation: Surface atomic structure and mechanistic considerations, J. Hazard. Mater. 424 (2022), 126786.

[11] Y. Zong, H. Zhang, Y. Shao, W. Ji, Y. Zeng, L. Xu, D. Wu, Surface-mediated periodate activation by nano zero-valent iron for the enhanced abatement of organic contaminants, J. Hazard. Mater. 423 (2022), 126991.

[12] L. He, L. Lv, S.C. Pillai, H. Wang, J. Xue, Y. Ma, Y. Liu, Y. Chen, L. Wu, Z. Zhang, L. Yang, Efficient degradation of diclofenac sodium by periodate activation using Fe/Cu bimetallic modified sewage sludge biochar/UV system, Sci. Total. Environ. 783 (2021) 146974.

[13] F. Liu, Y. Hou, S. Wang, Z. Li, B. Zhang, M. Tong, Periodate activation by pyrite for the disinfection of antibiotic-resistant bacteria: Performance and mechanisms, Water Res. 230 (2023) 119508.

[14] L. He, C. Yang, J. Ding, M.Y. Lu, C.X. Chen, G.Y. Wang, J.Q. Jiang, L. Ding, G.S. Liu, N.Q. Ren, S.S. Yang, Fe, N-doped carbonaceous catalyst activating periodate for micropollutant removal: Significant role of electron transfer, Appl. Catal. B: Environ. 303 (2022), 120880.

[15] C. Yang, Z.Z. Yang, K.H. Yang, Z.G. Yu, Y.Z. Zuo, L.J. Cheng, Y.B. Wang, H. Sun, G. L. Yu, C. Zhang, X. Li, Periodate activated by different crystalline phases MnO$_2$ for profound oxidation tetracycline hydrochloride: oxygen vacancy-dominated active pivots and mechanism, Sep. Purif. Technol. 301 (2022), 122022.

[16] J. Du, G. Xiao, Y. Xi, X. Zhu, F. Su, S.H. Kim, Periodate activation with manganese oxides for sulfanilamide degradation, Water Res. 169 (2020), 115278.

[17] Y.X. Gong, J.M. Shen, Y.N. Wu, L.L. Shen, S.X. Zhao, Y.C. Zhou, Y.B. Li, L. Cui, J. Kang, Z.L. Chen, Ligands-triggered evolution of catalytic intermediates during periodate activation via soluble Mn(II) for organic contaminants' abatement, Appl. Catal. B: Environ. 322 (2023), 122093.

[18] J.X. Yu, W. Qiu, X.C. Lin, Y.S. Wang, X.H. Lu, Y.B. Yu, H.T. Gu, S. Heng, H. C. Zhang, J. Ma, Periodate activation with stable MgMn$_2$O$_4$ spinel for bisphenol A removal: radical and non-radical pathways, Chem. Eng. J. 459 (2023), 141574.

[19] V.I. Parvulescu, F. Epron, H. Garcia, P. Granger, Recent progress and prospects in catalytic water treatment, Chem. Rev. 122 (2022) 2981–3121.

[20] Y. Yang, X. Li, C. Zhou, W. Xiong, G. Zeng, D. Huang, C. Zhang, W. Wang, B. Song, X. Tang, X. Li, H. Guo, Recent advances in application of graphitic carbon nitride-based catalysts for degrading organic contaminants in water through advanced oxidation processes beyond photocatalysis: a critical review, Water Res. 184 (2020), 116200.

[21] Z. Wang, C. Li, K. Domen, Recent developments in heterogeneous photocatalysts for solar-driven overall water splitting, Chem. Soc. Rev. 48 (2019) 2109–2125.

[22] Y. Wang, P. Du, H. Pan, L. Fu, Y. Zhang, J. Chen, Y. Du, N. Tang, G. Liu, Increasing solar absorption of atomically thin 2D carbon nitride sheets for enhanced visible-light photocatalysis, Adv. Mater. 31 (2019), e1807540.

[23] J.W. Fu, J.G. Yu, C.J. Jiang, B. Cheng, g-C$_3$N$_4$-based heterostructured photocatalysts, Adv. Energy Mater. 8 (2018) 1701503.

[24] F. Chen, L.L. Liu, J.J. Chen, W.W. Li, Y.P. Chen, Y.J. Zhang, J.H. Wu, S.C. Mei, Q. Yang, H.Q. Yu, Efficient decontamination of organic pollutants under high salinity conditions by a nonradical peroxymonosulfate activation system, Water Res. 191 (2021), 116799.

[25] F. Chen, L.L. Liu, J.H. Wu, X.H. Rui, J.J. Chen, Y. Yu, Single-atom iron anchored tubular g-C$_3$N$_4$ catalysts for ultrafast Fenton-Like reaction: roles of high-valent iron-oxo species and organic radicals, Adv. Mater. 34 (31) (2022), 2202891.

[26] K.A. Zhu, X.J. Chen, C.W. Yuan, C.W. Bai, Y.J. Sun, B.B. Zhang, F. Chen, Orientated construction of visible-light-assisted peroxymonosulfate activation system for antibiotic removal: significant enhancing effect of Cl$^-$, J. Hazard. Mater. 445 (2023), 130476.

[27] F. Wu, H.W. Huang, T.F. Xu, W.Y. Lu, N. Li, W.X. Chen, Visible-light-assisted peroxymonosulfate activation and mechanism for the degradation of pharmaceuticals over pyridyl-functionalized graphitic carbon nitride coordinated with iron phthalocyanine, Appl. Catal. B: Environ. 218 (2017) 230–239.

[28] Y. Chen, X.Z. Yuan, L.B. Jiang, Y.L. Zhao, H.Y. Chen, Z.C. Shangguan, C.C. Qin, H. Wang, Insights into periodate oxidation of antibiotics mediated by visible-light-induced polymeric carbon nitride: performance and mechanism, Chem. Eng. J. 457 (2023), 141147.

[29] J. Ding, W. Xu, H. Wan, D.S. Yuan, C. Chen, L. Wang, G.F. Guan, W.L. Dai, Nitrogen vacancy engineered graphitic C$_3$N$_4$-based polymers for photocatalytic oxidation of aromatic alcohols to aldehydes, Appl. Catal. B: Environ. 221 (2018) 626–634.

[30] J. Cao, W.S. Nie, L. Huang, Y.B. Ding, K.L. Lv, H.Q. Tang, Photocatalytic activation of sulfite by nitrogen vacancy modified graphitic carbon nitride for efficient degradation of carbamazepine, Appl. Catal. B: Environ. 241 (2019) 18–27.

[31] H. Yu, R. Shi, Y. Zhao, T. Bian, Y. Zhao, C. Zhou, G.I.N. Waterhouse, L.Z. Wu, C. H. Tung, T. Zhang, Alkali-assisted synthesis of nitrogen deficient graphitic carbon nitride with tunable band structures for efficient visible-light-driven hydrogen evolution, Adv. Mater. 29 (2017), 1605148.

[32] X.Y. Wang, J.Q. Meng, X.Y. Zhang, Y.Q. Liu, M. Ren, Y.X. Yang, Y.H. Guo, Controllable approach to carbon-deficient and oxygen-doped graphitic carbon nitride: robust photocatalyst against recalcitrant organic pollutants and the mechanism insight, Adv. Funct. Mater. 31 (2021), 2010763.

[33] L.L. Liu, F. Chen, J.H. Wu, M.K. Ke, C. Cui, J.J. Chen, H.Q. Yu, Edge electronic vacancy on ultrathin carbon nitride nanosheets anchoring O$_2$ to boost H$_2$O$_2$ photoproduction, Appl. Catal. B: Environ. 302 (2022), 120845.

[34] J. Jiang, Z. Zhao, J. Gao, T. Li, M. Li, D. Zhou, S. Dong, Nitrogen vacancy-modulated peroxymonosulfate nonradical activation for organic contaminant removal via high-valent cobalt-oxo species, Environ. Sci. Technol. 56 (2022) 5611–5619.

[35] B. Gao, G.Z. Chen, G. Li, Puma, Carbon nanotubes/titanium dioxide (CNTs/TiO$_2$) nanocomposites prepared by conventional and novel surfactant wrapping sol–gel methods exhibiting enhanced photocatalytic activity, Appl. Catal. B: Environ. 89 (2009) 503–509.

[36] D. Dolat, N. Quici, E. Kusiak-Nejman, A.W. Morawski, G. Li Puma, One-step, hydrothermal synthesis of nitrogen, carbon co-doped titanium dioxide (N,C-TiO$_2$) photocatalysts. Effect of alcohol degree and chain length as carbon dopant precursors on photocatalytic activity and catalyst deactivation, Appl. Catal. B: Environ. 115–116 (2012) 81–89.

[37] R. Acosta-Herazo, J. Monterroza-Romero, M.Á. Mueses, F. Machuca-Martínez, G. Li Puma, Coupling the six flux absorption–scattering model to the henyey–greenstein scattering phase function: evaluation and optimization of radiation absorption in solar heterogeneous photoreactors, Chem. Eng. J. 302 (2016) 86–96.

[38] R. Acosta-Herazo, M.Á. Mueses, G.L. Puma, F. Machuca-Martínez, Impact of photocatalyst optical properties on the efficiency of solar photocatalytic reactors rationalized by the concepts of initial rate of photon absorption (IRPA) dimensionless boundary layer of photon absorption and apparent optical thickness, Chem. Eng. J. 356 (2019) 839–849.

[39] L.B. Jiang, X.Z. Yuan, Y. Pan, J. Liang, G.M. Zeng, Z.B. Wu, H. Wang, Doping of graphitic carbon nitride for photocatalysis: a reveiw, Appl. Catal. B-Environ. 217 (2017) 388–406.

[40] H. Li, C. Shan, B. Pan, Fe(III)-doped g-C$_3$N$_4$ mediated peroxymonosulfate activation for selective degradation of phenolic compounds via high-valent iron-oxo species, Environ. Sci. Technol. 52 (2018) 2197–2205.

[41] T. Xiong, Y. Cen, Y. Zhang, F. Dong, Bridging the g-C$_3$N$_4$ interlayers for enhanced photocatalysis, ACS Catal. 6 (2016) 2462–2472.

[42] Y. Yang, G.M. Zeng, D.L. Huang, C. Zhang, D.H. He, C.Y. Zhou, W.J. Wang, W. P. Xiong, X.P. Li, B.S. Li, W.Y. Dong, Y. Zhou, Molecular engineering of polymeric carbon nitride for highly efficient photocatalytic oxytetracycline degradation and H$_2$O$_2$ production, Appl. Catal. B: Environ. 272 (2020), 118970.

[43] C.Y. Feng, L. Tang, Y.C. Deng, J.J. Wang, J. Luo, Y.N. Liu, X.L. Ouyang, H.R. Yang, J.F. Yu, J.J. Wang, Synthesis of Leaf-Vein-Like g-C$_3$N$_4$ with tunable band structures and charge transfer properties for selective photocatalytic H$_2$O$_2$ evolution, Adv. Func. Mater. 30 (2020), 2001922.

[44] W.J. Ong, L.L. Tan, Y.H. Ng, S.T. Yong, S.P. Chai, Graphitic carbon nitride (g-C$_3$N$_4$)-based photocatalysts for artificial photosynthesis and environmental remediation: are we a step closer to achieving sustainability? Chem. Rev. 116 (2016) 7159–7329.

[45] W. Liu, Y. Li, F. Liu, W. Jiang, D. Zhang, J. Liang, Visible-light-driven photocatalytic degradation of diclofenac by carbon quantum dots modified porous g-C$_3$N$_4$: Mechanisms, degradation pathway and DFT calculation, Water Res. 151 (2019) 8–19.

[46] F. Chen, G.X. Huang, F.B. Yao, Q. Yang, Y.M. Zheng, Q.B. Zhao, H.Q. Yu, Catalytic degradation of ciprofloxacin by a visible-light-assisted peroxymonosulfate activation system: Performance and mechanism, Water Res. 173 (2020), 115559.

[47] Y. Liu, Y. Zhao, J. Wang, Fenton/Fenton-like processes with in-situ production of hydrogen peroxide/hydroxyl radical for degradation of emerging contaminants: Advances and prospects, J. Hazard. Mater. 404 (2021), 124191.

[48] Y. Lei, Y. Yu, X. Lei, X. Liang, S. Cheng, G. Ouyang, X. Yang, Assessing the Use of Probes and Quenchers for Understanding the Reactive Species in Advanced Oxidation Processes, Environ. Sci. Technol. 57 (13) (2023) 5433–5444.

[49] Y.J. Zhang, G.X. Huang, L.R. Winter, J.J. Chen, L. Tian, S.C. Mei, Z. Zhang, F. Chen, Z.Y. Guo, R. Ji, Y.Z. You, W.W. Li, X.W. Liu, H.Q. Yu, M. Elimelech, Simultaneous nanocatalytic surface activation of pollutants and oxidants for highly efficient water decontamination, Nat. Commun. 13 (2022) 3005.